Biomineralization by particle attachment in early animals

Pupa U. P. A. Gilbert[a,b,c,d,1,2], Susannah M. Porter[e], Chang-Yu Sun[a], Shuhai Xiao[f], Brandt M. Gibson[g], Noa Shenkar[h,i], and Andrew H. Knoll[j,2]

[a]Department of Physics, University of Wisconsin–Madison, WI 53706; [b]Department of Chemistry, University of Wisconsin–Madison, WI 53706; [c]Department of Materials Science and Engineering, University of Wisconsin–Madison, WI 53706; [d]Department of Geoscience, University of Wisconsin–Madison, WI 53706; [e]Department of Earth Science, University of California, Santa Barbara, CA 93106; [f]Department of Geosciences, Virginia Tech, Blacksburg, VA 24061; [g]Department of Earth and Environmental Sciences, Vanderbilt University, Nashville, TN 37235; [h]School of Zoology, George S. Wise Faculty of Life Science, Tel-Aviv University, 69978 Tel Aviv, Israel; [i]The Steinhardt Museum of Natural History, National Research Center for Biodiversity Studies, Tel-Aviv University, 69978 Tel Aviv, Israel; and [j]Department of Organismic and Evolutionary Biology, Harvard University, Cambridge, MA 20138

Contributed by Andrew H. Knoll, July 4, 2019 (sent for review February 11, 2019; reviewed by Frédéric Marin and Tali Mass)

Crystallization by particle attachment (CPA) of amorphous precursors has been demonstrated in modern biomineralized skeletons across a broad phylogenetic range of animals. Precisely the same precursors, hydrated (ACC-H_2O) and anhydrous calcium carbonate (ACC), have been observed spectromicroscopically in echinoderms, mollusks, and cnidarians, phyla drawn from the 3 major clades of eumetazoans. Scanning electron microscopy (SEM) here also shows evidence of CPA in tunicate chordates. This is surprising, as species in these clades have no common ancestor that formed a mineralized skeleton and appear to have evolved carbonate biomineralization independently millions of years after their late Neoproterozoic divergence. Here we correlate the occurrence of CPA from ACC precursor particles with nanoparticulate fabric and then use the latter to investigate the antiquity of the former. SEM images of early biominerals from Ediacaran and Cambrian shelly fossils show that these early calcifiers used attachment of ACC particles to form their biominerals. The convergent evolution of biomineral CPA may have been dictated by the same thermodynamics and kinetics as we observe today.

biomineralization | calcium carbonate | skeleton | particle attachment

Crystallization by particle attachment (CPA) (1) was first observed in synthetic nanocrystalline titania (2), and, subsequently, in bacterial biominerals (3). A nonclassical crystallization mechanism (4), CPA is now known to occur, as well, during skeletal biomineralization, where amorphous particles attach first and crystallize later. Initially observed in sea urchin teeth (5), CPA of amorphous precursors has been demonstrated in modern biominerals across a broad phylogenetic range of animals, including sea urchin spicules (6), spines (7, 8), and teeth (5, 9); the larval shells (10) and nacre (11) of mollusks; zebrafish bone (12) and mouse enamel (13); and scleractinian coral skeletons (14). Echinoderms, mollusks, and cnidarians, drawn from the 3 major clades of eumetazoans, do not share a common biomineralizing ancestor; nonetheless, spectromicroscopic observations show that they use precisely the same precursors, hydrated (ACC-H_2O) and anhydrous amorphous calcium carbonate (ACC) (5, 11, 14–16). This is surprising because these groups diverged from one another in the Neoproterozoic Era, but they evolved their characteristic body plans and capacity for skeletal biomineralization only during the latest Ediacaran and Cambrian periods (17, 18). It would be intriguing, therefore, to know whether these mechanistic commonalities already existed in the earliest calcifying animals.

Fig. 1 presents an animal phylogeny, showing the broad but discontinuous phylogenetic distribution of animals with skeletons containing calcite, aragonite, or vaterite (the 3 polymorphs of anhydrous crystalline $CaCO_3$). The earliest known examples of $CaCO_3$ skeletal biomineralization occur in ca. 549 to 541 million year old (Ma) limestones around the world (19, 20), and by 535 to 510 Ma, calcareous skeletons referable to sponges, cnidarians, and extant bilaterian phyla formed globally (21, 22). The observation that skeletal growth by CPA of ACC precursors occurs in cnidarians, mollusks, and echinoderms raises the question of whether this mechanism is general, and if so, why, given that animals with carbonate skeletons have no common ancestor that was itself calcifying. Here we address this question by probing some of the oldest known examples of calcified skeletons, enabling us to ask whether the CPA–ACC mechanism evolved early in animal history. We focus on skeletons of the problematic, but arguably cnidarian genus *Cloudina* from terminal Ediacaran (549 to 541 Ma) rocks and lophotrochozoans (halkieriids and hyoliths) of middle Cambrian age (509 to 497 Ma). We examined specimens preserved by early diagenetic phosphatization, because this can preserve skeletal fabric in exquisite detail, revealing nanoscale features commonly obscured by recrystallization in calcareous specimens (23).

Results

CPA of ACC Precursors and Its Proxies. We hypothesize that $CaCO_3$ biomineralization has occurred by the attachment of amorphous particles since skeletal biomineralization first evolved, favored by thermodynamics and kinetics that we can observe today. We

Significance

The mechanisms by which organisms form mineralized skeletons have been a major research focus for the last 50 y and remain so today. Among the most surprising discoveries is the recent observation that different animals use the same mechanisms, and precisely the same amorphous precursors, to form biomineralized structures as diverse as coral skeletons, molluscan shells, and sea urchin spines. In living animals, skeletal biomineralization from amorphous precursors correlates with a distinctive nanoparticulate texture that can be preserved in fossils, enabling us to probe mechanisms of skeletal formation in early animals. We document nanoparticulate texture in some of the oldest known carbonate skeletons, which strongly suggests that skeletons formed from amorphous precursors throughout the recorded history of animals.

Author contributions: P.U.P.A.G. and A.H.K. designed research; P.U.P.A.G., C.-Y.S., and B.M.G. performed research; S.M.P., S.X., and N.S. contributed new reagents/analytic tools; P.U.P.A.G., S.M.P., C.-Y.S., S.X., B.M.G., and A.H.K. analyzed data; and P.U.P.A.G., S.M.P., S.X., and A.H.K. wrote the paper.

Reviewers: F.M., Université de Bourgogne–Franche-Comté; and T.M., University of Haifa.

Conflict of interest statement: P.U.P.A.G., C.-Y.S., and Tali Mass are coauthors on 2 research articles published in 2017.

[1]Previously published as Gelsomina De Stasio.

[2]To whom correspondence may be addressed. Email: pupa@physics.wisc.edu or aknoll@oeb.harvard.edu.

This article contains supporting information online at www.pnas.org/lookup/suppl/doi:10.1073/pnas.1902273116/-/DCSupplemental.

Published online August 19, 2019.

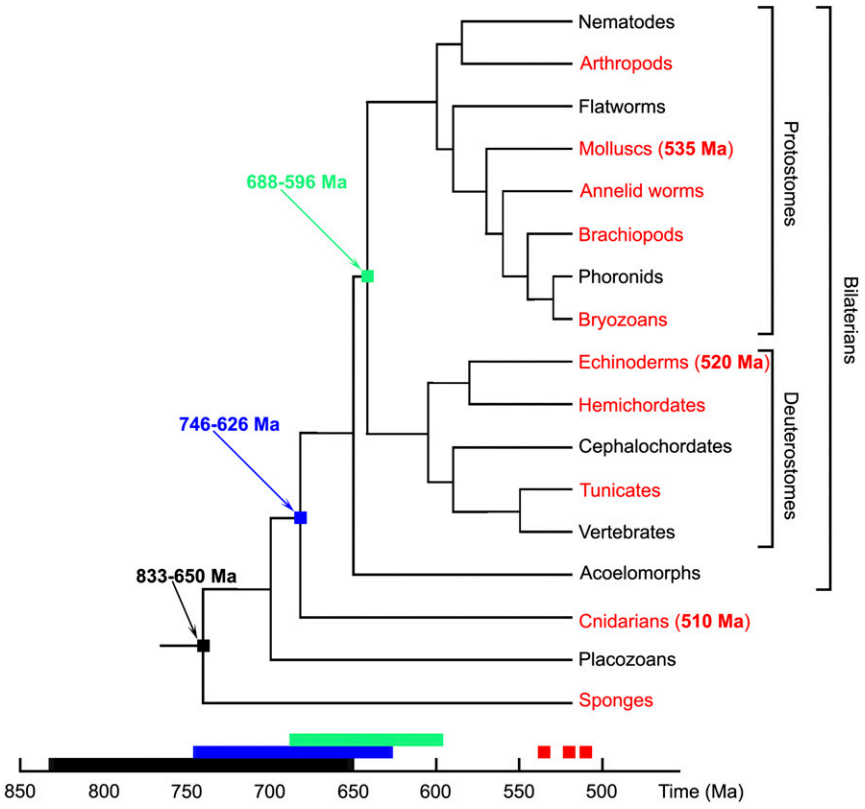

Fig. 1. A simplified phylogenetic tree of animals showing the distribution of $CaCO_3$ biomineralization. The major clades in which at least some members form $CaCO_3$ skeletons are highlighted in red. The phylogeny is after ref. 47. Dates in black, blue, or green are molecular clock estimates for early animal divergences (48, 49), and all nodes are positioned in time according to the molecular clock estimates from refs. 48, 49. Red dates in parentheses are the ages of the oldest fossils referable to the 3 principal phyla known to use ACC precursors in skeleton formation (mollusks, echinoderms, and cnidarians). The mollusk date comes from ref. 21, the cnidaria date is from ref. 22, and the echinoderm date is from ref. 50. Beyond any molecular clock uncertainties (48), the 3 phyla started biomineralizing long after diverging from one another.

know that the transformations from ACC-H_2O to ACC, and from ACC to calcite or aragonite, are exothermic reactions (24). Synthetic ACC-H_2O dehydrates and crystallizes within seconds, especially in contact with water; however, biogenic ACC-H_2O in animal skeletons takes 20 to 30 h to transform (11, 14, 15). The phases themselves are in energetically downhill sequence, but the longer times between phase transitions imply greater activation barriers between phases in vivo, likely offering the time required for greater physiological control of crystal morphology and orientation. To test whether early biomineralizers used the same mechanism of CPA of ACC precursors, we need to establish a physical proxy that can be preserved in ancient skeletons. Mastropietro et al. (25) argued that growth by amorphous particle attachment leaves a record in the form of a granular fabric observable via nanoscale imaging. Building on this, we correlated the complex and time-consuming synchrotron spectromicroscopy detection of ACC-H_2O and ACC in freshly formed biominerals (11, 14, 15) with observations from far simpler, and more widely available, scanning electron microscopy (SEM), confirming that the biominerals retain a nanoparticulate fabric after their ACC nanoparticles have filled space (26) and fully crystallized. In Figs. 2 and 3 we present evidence of this nanoparticulate fabric in modern biominerals, in which skeletal nanoparticles are 50 to 400 nm, consistent with many previous observations by SEM and coherence lengths measured by X-ray diffraction (27). The images also demonstrate that the nanoparticulate fabric differs from single-crystalline aragonite or calcite formed abiotically. Also in Fig. 2, we show nacre from molluscan shells of 4 different ages: Modern, Miocene (~13 Ma), Cretaceous (~100 Ma), and Late Ordovician (~450 Ma). The Miocene nacre is still aragonitic (28), and exhibits a nanoparticulate fabric comparable to that of modern nacre where tablets are fractured (arrows in Fig. 2 *A*–*E*). The Ordovician nacre was phosphatized during early diagenesis; as already observed by Mutvei (29) (cf. figures 2 and 3 in ref. 29 with Fig. 2*F* and *SI Appendix*, Fig. S1*F2*), it shows space between tablet layers, although tablets appear similar to modern nacre tablets from *Nautilus* after the latter are etched (29, 30), showing elongated nanocrystals oriented parallel to the tablet layers and radially distributed from the center of each tablet (cf. figure 4b in ref. 29 and figure 1b in ref. 30 with Fig. 2*F* and *SI Appendix*, S1 *F1* and *F2*).

In modern biominerals, nacre and sea urchin spines in particular, nanoparticles are cemented together and space filling (26); thus, it can be difficult to image them even after cryofracturing. However, it is clear that their cryofracture figures are neither cleavage planes nor conchoidal, as crystals or glass, respectively, typically break. Cryofractured biominerals exhibit irregular, rough fracture figures, as in fractured cement, sandstone, or any other granular materials. In order to more clearly reveal the nanoparticulate fabric of these modern biominerals, we partially etched them after cryofracturing and bleaching them. The results are shown in Fig. 2 *A* and *B* and Fig. 2*C* for *Haliotis* and *Nautilus* nacre, respectively, and in Fig. 3*A* for the sea urchin spine.

Importantly, the nanoparticulate fabric was clearly retained in the phosphatized nacre, even after fossil preparation and maceration. We note that Coronado et al. (31) documented a comparable granular nanofabric in (nonphosphatized) Devonian coral skeletons and interpreted it as evidence for skeletal growth by CPA of ACC. In contrast, nonbiogenic crystals of calcite, aragonite, and apatite do not exhibit the nanoparticulate texture observed in biominerals (Fig. 3 *C*–*F* and *SI Appendix*, Figs. S2 *C*–*F* and S6 *B2* and *C2*). We stress that the nanoparticles observed in modern biominerals are irregularly shaped—that is, noneuhedral–even though they become crystalline.

CPA in Vaterite Spicules from Tunicates. The comparison extends even to the third polymorph of $CaCO_3$, vaterite. It has been suggested (32) that outer spines of vaterite spicules from the ascidian tunicate *Herdmania momus* do not form via CPA because they cryofracture smoothly, akin to nonbiogenic single crystals. Here we reproduce this result with precisely the same magnification and conditions of all other experiments (Fig. 4*A*), but also show that at the forming end of the spicule the outer spines appear nanoparticulate and irregularly shaped (Fig. 4*B*). At a

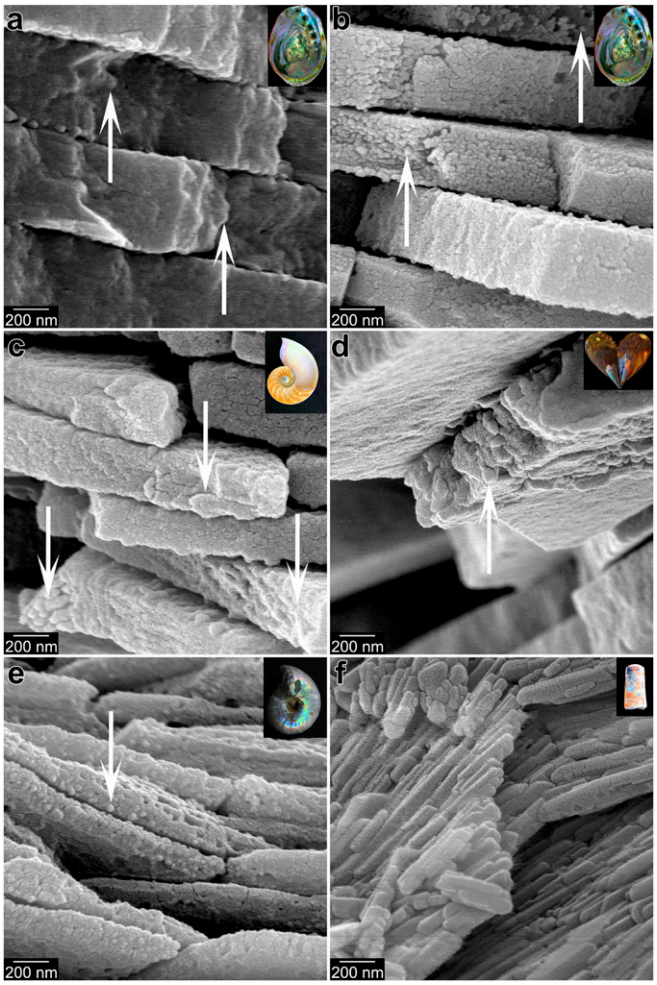

Fig. 2. Modern and fossil nacre from 3 molluscan classes, exhibiting irregularly shaped nanoparticles. Arrows indicate fractured tablets. (*A*) Cryofractured modern nacre from the gastropod *Haliotis rufescens*. (*B*) Nacre as in *A*, but bleached and etched to better reveal its nanoparticulate texture. (*C*) Nacre from the modern cephalopod *Nautilus pompilius*, cryofractured, bleached, etched. (*D*) Nacre from the Miocene (~13 Ma) bivalve *Atrina harrisii* nacre, which is still 100% aragonite (28). (*E*) Nacre from a Cretaceous (~100 Ma) ammonite *Desmoceras* sp. (*F*) Nacre from the Upper Ordovician (~450 Ma) cephalopod *Isorthoceras sociale* nacre, which is secondarily phosphatized. Lower-magnification, cocentered images from the same locations as these are presented in *SI Appendix*, Fig. S1, where they are correspondingly labeled. *Insets* show photographs of similar samples.

later stage, their morphology is euhedral, and specifically hexagonal pyramidal (Fig. 4*A*), possibly because of a dissolution and (re)crystallization process (33). The inner core of the vaterite spicule remains nanoparticulate and cryofractures accordingly at all stages (Fig. 4*C*). Thus, tunicates—which evolved biomineralization independently of other clades discussed here and diverged from their closest biomineralizing relatives, the vertebrates, no later than the early Cambrian Period (Fig. 1 and references therein)—show evidence of skeletal mineralization by particle attachment.

Evidence of CPA in Ediacaran and Cambrian Phosphatized Fossils. Armed with the observations that CPA of ACC-H_2O and ACC precursors in modern biominerals correlate with nanoparticulate fabric at the SEM level, and that diagenetic phosphatization does not alter this fabric (Fig. 2*F* and *SI Appendix*, Fig. S1*F*), we can use it as a proxy for CPA of ACC-H_2O and ACC in skeletal biominerals from Ediacaran and Cambrian animals.

Fig. 5 and *SI Appendix*, Fig. S5 show nanoparticulate fabrics in a phosphatized *Cloudina* specimen (*Cloudina* 111–2) from the terminal Ediacaran (551 to 541 Ma) Dengying Formation in South China (34). The specimen was imaged using SEM and X-ray microcomputed tomography (*SI Appendix*, Fig. S3 and *Cloudina*. mov, a movie also in *SI Appendix*), and was then fractured (*SI Appendix*, Fig. S4) and imaged again using high-resolution SEM. The fractured cross-section of the shell exhibits irregularly shaped 50- to 400-nm nanoparticles (Fig. 5 and *SI Appendix*, Fig. S5). This nanoparticulate fabric is distinct from the smooth appearance of a nonbiogenic apatite crystal (Fig. 3*D* and *SI Appendix*, Fig. S2 *C–F*) and is confirmed in multiple cross-section regions within 2 specimens from the same population (*SI Appendix*, Figs. S3 and S4), although one fossil shows localized recrystallization (e.g., *SI Appendix*, Fig. S6*A*). Indeed, recrystallization is prevalent in nonphosphatized *Cloudina* skeletons (e.g., those from Namibia; *SI Appendix*, Fig. S6*B*), showing the advantages of phosphatized specimens. We note that, although the size range is the same in modern skeletons and

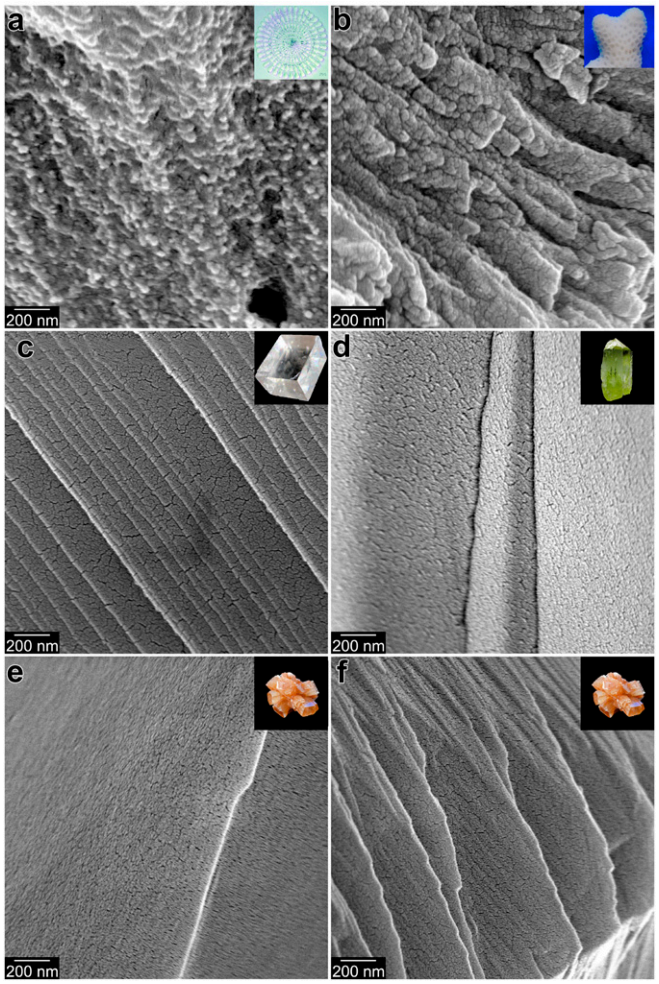

Fig. 3. Modern biominerals and nonbiogenic mineral crystals, all cryofractured. The biominerals exhibit irregularly shaped nanoparticulate fracture figures, whereas the nonbiogenic minerals show smooth, flat fracture figures. (*A*) Modern *Strongylocentrotus purpuratus* sea urchin spine, cryofractured and etched to reveal its nanoparticulate texture. (*B*) Modern *Stylophora pistillata* coral skeleton. (*C*) Nonbiogenic calcite. (*D*) Nonbiogenic apatite. Nonbiogenic aragonite, with typical featureless appearance (*E*) and rare feature-rich surface (*F*). The cracked appearance on all smooth, flat surfaces in *C–F* originates from the 20-nm Pt coating. Lower-magnification, cocentered, colabeled images from these locations are presented in *SI Appendix*, Fig. S2. *Insets* show photographs of similar samples.

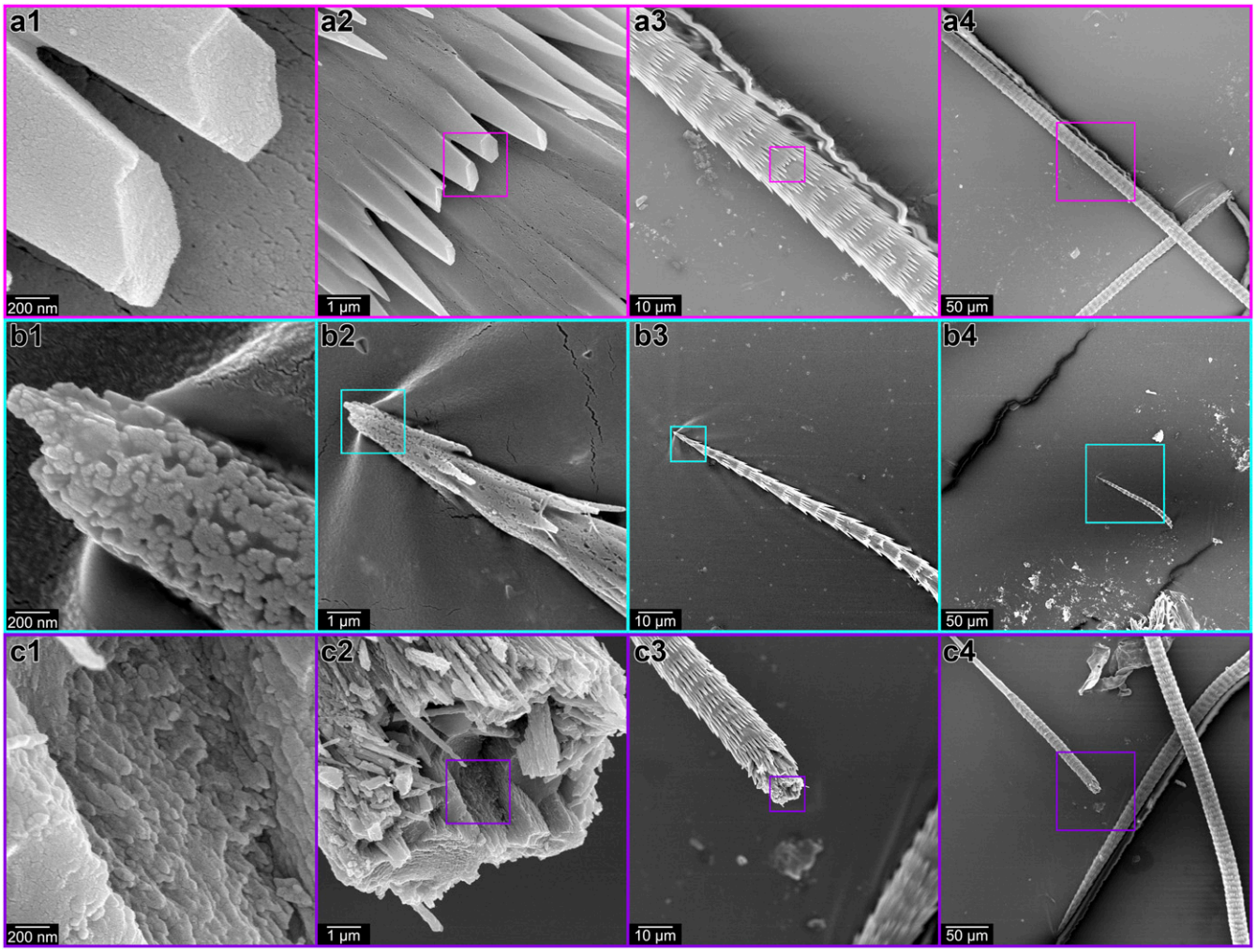

Fig. 4. Modern vaterite spicule from the ascidian tunicate *Herdmania momus*. (*A*) Hexagonal pyramidal outer spines, exhibiting a smooth cryofracture figure. (*B*) The forming end of another vaterite spicule, in which both the outer spines and the inner core appear nanoparticulate. (*C*) The inner core of a third vaterite spicule, exhibiting a nanoparticulate cryofracture figure. Boxes in panels 2, 3, 4 indicate the area magnified in panels 1, 2, 3.

Cloudina specimens, the average size is slightly larger in *Cloudina*. This could have been the original size or reflect diagenetic coarsening.

In Fig. 6 we present a hyolith conch (35) and a halkieriid sclerite (36), from the middle Cambrian Gowers and Monastery Creek formations, Georgina Basin, Australia, respectively, both phosphatized during early diagenesis. *SI Appendix*, Fig. S7 shows these small shelly fossils before and after fracturing. Note in Fig. 6 and *SI Appendix*, Fig. S7 the 50- to 400-nm nanofilaments in the hyolith and 50- to 400-nm rounded nanoparticles in the halkieriid cross section. *SI Appendix*, Fig. S8 *A–D* shows a variety of elongated spherulitic or euhedral crystals in the internal mold or the wall cross-section of other sclerites, whereas *SI Appendix*, Fig. S8*E* shows the globular nanoparticulate phosphatized outer layer of a halkieriid sclerite, interpreted as an originally organic layer akin to the periostracum that lines the outer surface of modern molluscan shells (36). As in *Cloudina*, small shelly fossils occasionally show recrystallization, forming nano- or microscale euhedral crystals (*SI Appendix*, Fig. S8). Recrystallization is sporadically observed in the shells of middle Cambrian mollusks and the sclerites of chancelloriids (*SI Appendix*, Figs. S8*A* and S9 *B* and *C*). When well-preserved, phosphatized fossils lack any euhedral crystals, at any magnification (e.g., Fig. 6 and *SI Appendix*, Fig. S7) exhibiting only irregularly shaped nanoparticulate texture.

Since the internal mold in *SI Appendix*, Fig. S8*D* and the outer layer akin to a periostracum in *SI Appendix*, Fig. S8*E* both appear nanoparticulate in cross-section, we speculate that both minerals precipitated in the presence of abundant organic molecules, from the decaying halkieriid or its periostracum, and this made them precipitate as nanoparticles. Since these nanoparticles were not deposited by the animal as ACC, they differ morphologically: they are globular where the periostracum was, and euhedral hexagonal prisms in the internal mold. This tentative interpretation is also supported by the observation that most of the recrystallized fossils and their internal molds shown here are euhedral nanoparticulate (halkieriid in *SI Appendix*, Fig. S8 *A–C*; nacre in *SI Appendix*, Fig. S9*A*; and chancelloriid in *SI Appendix*, Fig. S9*B*). In these cases, the presence of organics may have made apatite crystals nanoscaled, but more regularly shaped: either euhedral or spherical.

Discussion

Figs. 2–6 demonstrate that the nanoparticulate fabric associated with CPA of ACC particles in modern calcifying animals extends back to the earliest record of skeletal biomineralization in Ediacaran and Cambrian fossils. Ion exchange, which substitutes one ion at a time, has been extensively characterized at the macroscale (37), and more recently at the nano- (38–40) and microscales (41). Both nano- and microscale structures (41) retain

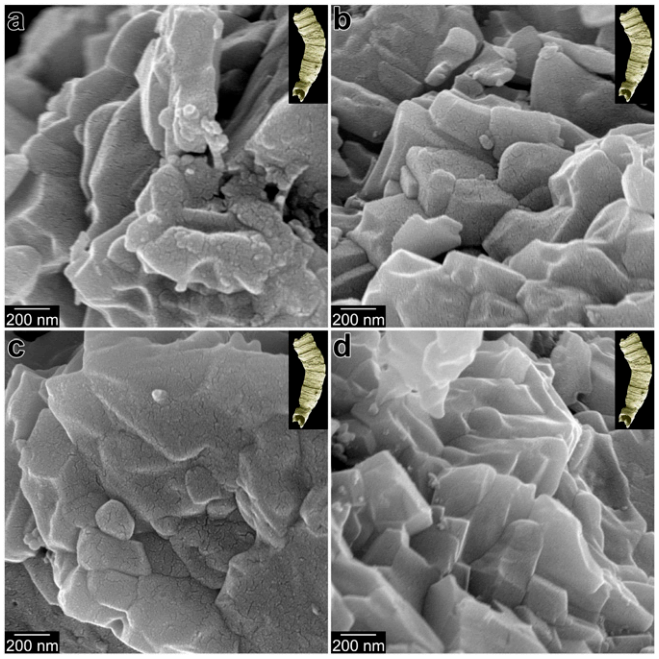

Fig. 5. Irregularly shaped nanoparticles in the fractured walls of phosphatized Ediacaran (~550 Ma) *Cloudina* skeletons. Lower-magnification, cocentered, colabeled images from these locations are presented in *SI Appendix*, Fig. S5.

their original shape and size after ion exchange has occurred. It is therefore reasonable to conclude that the phosphatized fossils observed here underwent a similar fabric-retentive transformation. After such pseudomorphic transformations, the crystal habit of the previous mineral, not the transformed one, is usually observed (e.g., *SI Appendix*, Figs. S9 *B1* and *B2*, which is now apatite but retains a calcite crystal habit). Unusually, the fabric of the well-preserved phosphatized fossils presented here did not include euhedral crystals, but irregular, noneuhedral particles on the order of 50- to 400-nm in size. Phosphates formed by other processes, for example, nonbiogenic apatite (Fig. 3*D* and *SI Appendix*, Fig. S2*D*) or internal molds formed after the death of the animal (*SI Appendix*, Fig. S8 *B–D*), do not show the same fabric. We conclude, therefore, that animals used CPA of ACC precursor particles to form $CaCO_3$ skeletons at the inception of biomineralization in each lineage, *Cloudina*, halkieriids, and hyoliths, and tentatively suggest that they have ever since taken advantage of the same thermodynamics (24) and kinetics (42) as modern calcifying animals do (15).

The physical chemistry of ACC in confinement was first explored about a decade ago (43), and recent experiments on its crystallization kinetics suggest that ACC confined to a volume of 0.1 μm^3 is stable, not crystallizing to calcite on timescales of up to 10^6 y (42). The nanoparticles observed here in all biominerals, ranging in size between 50 and 400 nm, occupy volumes 0.0005 to 0.3 μm^3; thus, they should be comparably stable, assuming that the nanoparticles were originally ACC and were confined to similar volumes within cells. This suggests that the ACC precursor phase was selected multiple times in the history of biomineralization, at least in part because of its stability when confined and its capacity to crystallize once released from confinement. For a biomineralizing animal, crystallization to the wrong polymorph, or at the wrong time or location would be detrimental; thus, a stable precursor phase is necessary for biomineralization. Also, stabilization by confinement, rather than by proteins, is fully reversible, providing additional benefits to biomineralizing animals. As yet, there is no consensus on why animal biomineralization proceeds by attachment of amorphous particles, but the kinetic advantage of confinement provides one promising hypothesis; other, potentially complementary, avenues to explore include both growth rate and fine control on morphogenesis.

Materials and Methods

Modern Biomineral and Fossil Samples. In order of appearance in the main text, all samples are as follows: Fig. 2*A* and *SI Appendix*, Fig. S1*A*: Modern red abalone (*Haliotis rufescens*) from Monterey Abalone Company, Monterey, CA, cryofractured in liquid nitrogen (LN_2), thermalized in ethanol, air dried, and Pt-coated.

Fig. 2*B* and *SI Appendix*, Fig. S1*B*: Modern red abalone (*Haliotis rufescens*) from Monterey Abalone Company, Monterey, CA, 100 mm in length, was notched, cryofractured in LN_2, thermalized in ethanol, bleached for 1 h in 6% NaClO, rinsed twice in DD H_2O at pH 8, etched for 2 s in 1 v% acetic acid, rinsed twice in DD H_2O at pH 8, rinsed in ethanol, air dried, and Pt-coated.

Fig. 2*C* and *SI Appendix*, Fig. S1*C*: Modern *Nautilus pompilius* shell (141.8 mm length) originated off the coast of Jolo Island, Philippines. It was notched, cryofractured in LN_2, thermalized in ethanol, bleached for 1 h in 6% NaClO, rinsed twice in DD H_2O at pH 8, etched for 2 s in 1 v% acetic acid, rinsed twice in DD H_2O at pH 8, rinsed in ethanol, air dried, and Pt-coated.

Fig. 2*D* and *SI Appendix*, Fig. S1*D*: Miocene (~13 Ma) nacre from *Atrina harrisii*, Choptank Fm, Calvert, MD.

Fig. 2*E* and *SI Appendix*, Fig. S1*D*: Cretaceous, Albian (~100 Ma) ammonite *Desmoceras* sp. was found in Mitsinjo near Majunga, Northwest Madagascar. A nacre fragment was notched, cryofractured in LN_2, thermalized in ethanol, bleached for 1 h in 6% NaClO, rinsed twice in DD H_2O at pH 8, etched for 1 s in 1 v% acetic acid, rinsed twice in DD H_2O at pH 8, rinsed in ethanol, air dried, and Pt-coated.

Fig. 2*F* and *SI Appendix*, Fig. S1*F*: Upper Ordovician (~450 Ma) nacre from *Isorthoceras sociale* from Maquoketa Formation, Graf, IA. This nacre is completely phosphatized, and extracted by maceration in 5 to 10 v% acetic acid for a few days, thus any residual aragonite was removed.

Fig. 3*A* and *SI Appendix*, Fig. S2*A*: Modern sea urchin spine from *Strongylocentrotus purpuratus,* from Bodega Marine Laboratory, Bodega Bay, CA. The spine was notched, cryofractured in LN_2, thermalized in ethanol, bleached for 1 h in 6% NaClO, rinsed twice in DD H_2O at pH 8, etched for 10 min in 1 v% acetic acid, rinsed twice in DD H_2O at pH 8, rinsed in ethanol, air dried, and Pt-coated.

Fig. 3*B* and *SI Appendix*, Fig. S2*B*: Cryofractured modern coral skeleton from *Stylophora pistillata* from Albany Aquarium, Albany, CA. Fig. 3*C* and

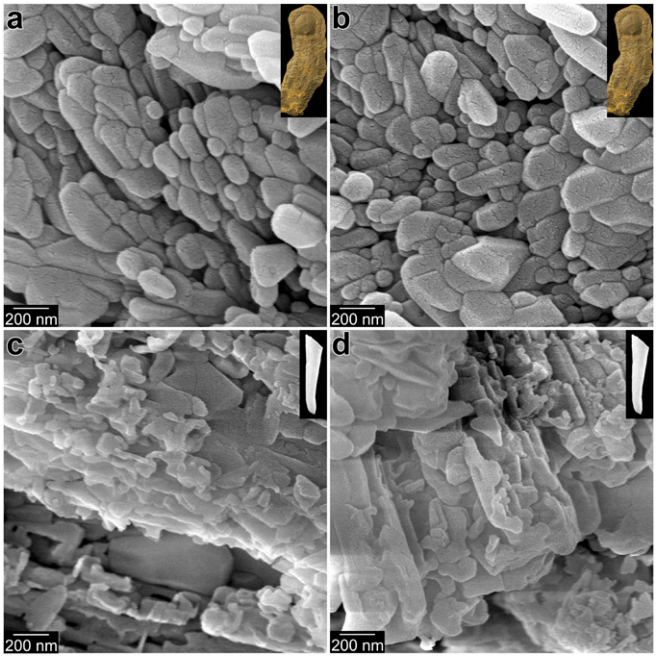

Fig. 6. Cambrian phosphatized small shelly fossils after fracturing. (*A* and *B*) Halkieriid sclerite. (*C* and *D*) Hyolith conch. All 4 cross-sections show irregularly shaped, noneuhedral nanoparticles. Lower-magnification, cocentered, colabeled images from these locations and others are presented in *SI Appendix*, Fig. S7. Additional data in *SI Appendix*, Fig. S8.

SI Appendix, Fig. S2*C*: Cryofractured geologic, nonbiogenic calcite (Snarum, Norway). Fig. 3*D* and *SI Appendix*, Fig. S2*D*: Cryofractured geologic, nonbiogenic apatite (Durango, Mexico). Fig. 3 *E* and *F* and *SI Appendix*, Fig. S2 *E* and *F*: Cryofractured geologic, nonbiogenic aragonite (Sefrou, Morocco)

Fig. 4: Modern vaterite spicules from the tunicate *Herdmania momus* from the Steinhardt Museum of Natural History, Tel-Aviv, Israel. The tunicates were collected in 2004 in Eilat, Israel, at a depth of 15 m, and preserved in ethanol until May 2019. The spicules were extracted by bleaching 2 entire tunicates for 5 d, then harvesting them from the bottom with a pipette. The spicules were rinsed in ethanol 5 times, then collected individually, placed on carbon tape, and cryofractured in LN_2, thermalized in ethanol, air dried, and Pt-coated.

Fig. 5 and *SI Appendix*, Fig. S3–S5: Phosphatized *Cloudina* specimen 111–2, from the terminal Ediacaran (551–541 Ma) Dengying Formation, Lijiagou, South China.

SI Appendix, Fig. S6*A*: Phosphatized *Cloudina* specimen 102–1, from the terminal Ediacaran (551–541 Ma) Dengying Formation, Lijiagou, South China.

SI Appendix, Fig. S6*B*: This is a third *Cloudina* sample from a patch reef exposed on Donkergange Farm, Omkyk Member of the Zaris Formation, Nama Group, Namibia, which was completely recrystallized and not phosphatized. This sample did not show any irregularly shaped nanoparticles, either after room temperature fracturing or cryofracturing.

SI Appendix, Fig. S6*C*: Geologic calcite cryofractured in mortar and pestle.

Fig. 6 *A* and *B* and *SI Appendix*, Fig. S7 *A* and *B*: *Australohalkieria superstes* halkieriid sclerite from the middle Cambrian Monastery Creek Formation, Georgina Basin, Australia.

Fig. 6 *C* and *D* and *SI Appendix*, Fig. S7 *C* and *D*: A hyolith (species undetermined) from the middle Cambrian Gowers Formation, Georgina Basin, Australia.

SI Appendix, Fig. S8 *A*, *B*, and *C*–*E*: Three different sclerites from *Australohalkieria superstes* from the Middle Cambrian Monastery Creek Formation, Georgina Basin, Australia.

SI Appendix, Fig. S9*A*: *Isorthoceras sociale*, from Maquoketa Formation, Graf, IA. This Upper Ordovician nacre is completely phosphatized and was extracted by maceration in 5–10 v% acetic acid for a few days, removing any residual aragonite. This is from a very curved part of the septum and totally recrystallized.

SI Appendix, Fig. S9*B*: Sclerite from the chancelloriid *Archiasterella hirundo* from the lower Cambrian Parara Limestone, Yorke Peninsula, South Australia (44, 45).

SI Appendix, Fig. S9*C*: The mollusk *Yochelcionella snorkorum*, from the middle Cambrian Gowers Formation, Australia (46).

Nonbiological Mineral Samples. Single crystal aragonite (from Sefrou, Morocco), calcite (from Brazil), and apatite (from Durango, Mexico) were acquired from Ward's Science.

Sample Preparation. Ediacaran and Cambrian skeletal fossils were extracted using standard acetic acid maceration techniques: immersing the rocks into 5 to 10 v% acetic acid for a few days. Fossils were then handpicked from maceration residues under a binocular microscope.

Before being fractured, the *Cloudina* specimens 111–2 (*SI Appendix*, Fig. S3*A*) and 102–1 were imaged on an FEI Quanta 600 FEG environmental SEM (at 20 kV and in secondary electron mode) in the Nanoscale Characterization and Fabrication Laboratory at Virginia Tech. Specimen 111–2 was scanned on an Xradia Micro-CT scanner at Virginia Tech and also on a North Star Imaging ImagiX Micro-CT scanner at Vanderbilt University (123 kV with 4.1 μm/voxel). Scan data were reconstructed and processed in efX-CT 1.9.5.12 (*SI Appendix*, Fig. S3 *B* and *C*). Hyolith, halkieriid, and mollusk specimens were imaged on a FEI Quanta 400F environmental SEM at 5.0 kV and 9 mm working distance at the Department of Earth Science, University of California, Santa Barbara.

All fossil biominerals were fractured at room temperature (RT), and only cross-sections fractured by us were analyzed, to avoid secondary overgrowth or contaminants that precipitated or were deposited on the shell surfaces during geologic time or during sample preparation.

All geologic minerals and modern biominerals were cryofractured to minimize cleavage and prevent smearing. To cryofracture them at predictable locations, and at the desired size compatible with SEM mounting, all samples were notched on 3 sides using a diamond saw, with water as a lubricant and coolant. They were then rinsed in DD water, then ethanol, and air dried overnight. They were then immersed in liquid nitrogen, let thermalize, and fractured with a microscalpel at the notches, to reveal a cryofractured surface. They were then immediately removed from liquid nitrogen and immersed in ethanol for 15 to 30 min to let them return to RT while preventing condensation of atmospheric water vapor on their cold surfaces.

In addition, a calcite specimen was cryofractured in an agate mortar and pestle, after flooding the mortar and pestle with liquid nitrogen. One of the grains in this sample exhibited the more feature-rich appearance shown in *SI Appendix*, Fig. S6*B*.

Modern biominerals were also gently etched, to better reveal their nanoparticulate fracture figures. Etching was done using 1 v% acetic acid for 1 to 2 s for nacre from modern *Haliotis rufescens* and *Nautilus pompilius*, ammonite *Desmoceras* sp. and Miocene *Atrina harrisii*, and for coral skeletons, as well as nonbiogenic aragonite. Etching was done for 1 to 20 min for *Strongylocentrotus purpuratus* spines. Before etching, these samples were cryofractured as described above, bleached for 1 h in 6% NaOCl, rinsed twice in DD-H_2O at pH 8.0. The *Haliotis rufescens*, *Nautilus pompilius,* and ammonite *Desmoceras* sp. samples in Fig. 2 *B*, *C*, and *E* were then etched for 2 s. The *Strongylocentrotus purpuratus* spine sample selected for Fig. 3*A* was etched for 10 min. The coral sample is presented unetched, as its nanoparticles are clearly visible even before etching.

All samples were magnetron sputter-coated with 20 nm Pt while rotating and tilting the sample, using a Cressington 208 HR sputter coater (Ted Pella). This thicker than normal coating, combined with tilting and rotation during coating greatly reduced charging artifacts, which otherwise would have made the experiments impossible in fractured samples with great topographic relief as those analyzed here. We note that such thick coating could in principle hide nanoparticles smaller than 20 nm, but such particles, when they protrude on the surface of fractured biominerals, are still clearly visible in Figs. 2, 3, 5, and 6.

All samples were analyzed using a Hitachi S5000 SEM at the Electron Microscopy Laboratory at University of California, Berkeley, CA. The microscope was operated at 10 kV, in secondary electron mode. All samples were focused at 450,000×, then imaged at 100,000×, 50,000×, 10,000×, 1,000×, and 250×.

The images in *SI Appendix*, Fig. S4 *E*, *H*, and *I* were acquired using a Hitachi TM1000 SEM, also at EML. This instrument operates at 15 kV, in backscattered electron mode. All figures were assembled in Adobe Photoshop CC 2017. The only image manipulation done was "auto-level" in Photoshop, to adjust brightness and contrast. Arrows and labels were also added in Photoshop.

ACKNOWLEDGMENTS. We thank Steve Weiner and 2 reviewers for reading and constructively criticizing the manuscript. We thank Guangwei Min for technical assistance during SEM experiments; Yaoping Cai, Ivan Cortijo, Hong Hua, and John Moore for assistance in field work and fossil extraction; John Nance and Robert Hazen for the Miocene nacre samples. P.U.P.A.G. acknowledges support from the US Department of Energy, Office of Science, Office of Basic Energy Sciences, Chemical Sciences, Geosciences, and Biosciences Division, under Award DE-FG02-07ER15899, and NSF grant DMR-1603192.

1. J. J. De Yoreo *et al*., Crystallization by particle attachment in synthetic, biogenic, and geologic environments. *Science* **349**, aaa6760 (2015).
2. R. L. Penn, J. F. Banfield, Oriented attachment and growth, twinning, polytypism, and formation of metastable phases: Insights from nanocrystalline TiO_2. *Am. Mineral.* **83**, 1077–1082 (1998).
3. J. F. Banfield, S. A. Welch, H. Zhang, T. T. Ebert, R. L. Penn, Aggregation-based crystal growth and microstructure development in natural iron oxyhydroxide biomineralization products. *Science* **289**, 751–754 (2000).
4. M. Niederberger, H. Cölfen, Oriented attachment and mesocrystals: Non-classical crystallization mechanisms based on nanoparticle assembly. *Phys. Chem. Chem. Phys.* **8**, 3271–3287 (2006).
5. C. E. Killian *et al*., Mechanism of calcite co-orientation in the sea urchin tooth. *J. Am. Chem. Soc.* **131**, 18404–18409 (2009).
6. E. Beniash, J. Aizenberg, L. Addadi, S. Weiner, Amorphous calcium carbonate transforms into calcite during sea urchin larval spicule growth. *Proc. R. Soc. Lond. B Biol. Sci.* **264**, 461–465 (1997).
7. Y. Politi, T. Arad, E. Klein, S. Weiner, L. Addadi, Sea urchin spine calcite forms via a transient amorphous calcium carbonate phase. *Science* **306**, 1161–1164 (2004).
8. M. Albéric *et al*., Growth and regrowth of adult sea urchin spines involve hydrated and anhydrous amorphous calcium carbonate precursors. *J. Struct. Biol.* **1**, 100004 (2019).
9. C. E. Killian *et al*., Self-sharpening mechanism of the sea urchin tooth. *Adv. Funct. Mater.* **21**, 682–690 (2011).
10. I. M. Weiss, N. Tuross, L. Addadi, S. Weiner, Mollusc larval shell formation: Amorphous calcium carbonate is a precursor phase for aragonite. *J. Exp. Zool.* **293**, 478–491 (2002).

11. R. T. DeVol *et al*., Nanoscale transforming mineral phases in fresh nacre. *J. Am. Chem. Soc.* **137**, 13325–13333 (2015).
12. J. Mahamid, A. Sharir, L. Addadi, S. Weiner, Amorphous calcium phosphate is a major component of the forming fin bones of zebrafish: Indications for an amorphous precursor phase. *Proc. Natl. Acad. Sci. U.S.A.* **105**, 12748–12753 (2008).
13. E. Beniash, R. A. Metzler, R. S. Lam, P. U. Gilbert, Transient amorphous calcium phosphate in forming enamel. *J. Struct. Biol.* **166**, 133–143 (2009).
14. T. Mass *et al*., Amorphous calcium carbonate particles form coral skeletons. *Proc. Natl. Acad. Sci. U.S.A.* **114**, E7670–E7678 (2017).
15. Y. U. T. Gong *et al*., Phase transitions in biogenic amorphous calcium carbonate. *Proc. Natl. Acad. Sci. U.S.A.* **109**, 6088–6093 (2012).
16. Y. Politi *et al*., Transformation mechanism of amorphous calcium carbonate into calcite in the sea urchin larval spicule. *Proc. Natl. Acad. Sci. U.S.A.* **105**, 17362–17366 (2008).
17. A. H. Knoll, Biomineralization and evolutionary history. *Rev. Mineral. Geochem.* **54**, 329–356 (2003).
18. D. J. Murdock, P. C. Donoghue, Evolutionary origins of animal skeletal biomineralization. *Cells Tissues Organs* **194**, 98–102 (2011).
19. S. W. Grant, Shell structure and distribution of *Cloudina*, a potential index fossil for the terminal Proterozoic. *Am. J. Sci.* **290-A**, 261–294 (1990).
20. J. P. Grotzinger, W. A. Watters, A. H. Knoll, Calcified metazoans in thrombolite-stromatolite reefs of the terminal Proterozoic Nama Group, Namibia. *Paleobiology* **26**, 334–359 (2000).
21. S. M. Porter, Calcite and aragonite seas and the *de novo* acquisition of carbonate skeletons. *Geobiology* **8**, 256–277 (2010).
22. T. Y. Park *et al*., A stem-group cnidarian described from the mid-Cambrian of China and its significance for cnidarian evolution. *Nat. Commun.* **2**, 442 (2011).
23. B. Runnegar, Shell microstructures of Cambrian molluscs replicated by phosphate. *Alcheringa* **9**, 245–257 (1985).
24. A. V. Radha, T. Z. Forbes, C. E. Killian, P. U. P. A. Gilbert, A. Navrotsky, Transformation and crystallization energetics of synthetic and biogenic amorphous calcium carbonate. *Proc. Natl. Acad. Sci. U.S.A.* **107**, 16438–16443 (2010).
25. F. Mastropietro *et al*., Revealing crystalline domains in a mollusc shell single-crystalline prism. *Nat. Mater.* **16**, 946–952 (2017).
26. L. Yang, C. E. Killian, M. Kunz, N. Tamura, P. U. P. A. Gilbert, Biomineral nanoparticles are space-filling. *Nanoscale* **3**, 603–609 (2011).
27. A. Gal *et al*., Particle accretion mechanism underlies biological crystal growth from an amorphous precursor phase. *Adv. Funct. Mater.* **24**, 5420–5426 (2014).
28. P. U. P. A. Gilbert *et al*., Nacre tablet thickness records formation temperature in modern and fossil shells. *Earth Planet. Sci. Lett.* **460**, 281–292 (2017).
29. H. Mutvei, Flexible nacre in the nautiloid *Isorthoceras*, with remarks on the evolution of cephalopod nacre. *Lethaia* **16**, 233–240 (1983).
30. A. G. Checa *et al*., Crystallographic control on the substructure of nacre tablets. *J. Struct. Biol.* **183**, 368–376 (2013).
31. I. Coronado, A. Pérez-Huerta, S. Rodríguez, Analogous biomineralization processes between the fossil coral *Calceola sandalina* (Rugosa, Devonian) and other recent and fossil cnidarians. *J. Struct. Biol.* **196**, 173–186 (2016).
32. B. Pokroy *et al*., Narrowly distributed crystal orientation in biomineral vaterite. *Chem. Mater.* **27**, 6516–6523 (2015).
33. H. Du, E. Amstad, Water: How does it influence the $CaCO_3$ formation? *Angew. Chem. Int. Ed. Engl.* 10.1002/anie.201903662 (2019).
34. I. Cortijo, Y. Cai, H. Hua, J. D. Schiffbauer, S. Xiao, Life history and autecology of an Ediacaran index fossil: Development and dispersal of *Cloudina*. *Gondwana Res.* **28**, 419–424 (2015).
35. J. Moore, S. M. Porter, Plywood-like shell microstructures in hyoliths from the middle Cambrian (Drumian) Gowers Formation, Georgina Basin, Australia. *Palaeontology* **61**, 441–467 (2018).
36. S. M. Porter, Halkieriids in middle Cambrian phosphatic limestones from Australia. *J. Paleontol.* **78**, 574–590 (2004).
37. F. G. Helfferich, *Ion Exchange* (Courier Corporation, 1995).
38. D. H. Son, S. M. Hughes, Y. Yin, A. Paul Alivisatos, Cation exchange reactions in ionic nanocrystals. *Science* **306**, 1009–1012 (2004).
39. J. M. Hodges, K. Kletetschka, J. L. Fenton, C. G. Read, R. E. Schaak, Sequential anion and cation exchange reactions for complete material transformations of nanoparticles with morphological retention. *Angew. Chem. Int. Ed. Engl.* **54**, 8669–8672 (2015).
40. I. T. Sines *et al*., Engineering porosity into single-crystal colloidal nanosheets using epitaxial nucleation and chalcogenide anion exchange reactions: The conversion of SnSe to SnTe. *Chem. Mater.* **24**, 3088–3093 (2012).
41. T. Holtus *et al*., Shape-preserving transformation of carbonate minerals into lead halide perovskite semiconductors based on ion exchange/insertion reactions. *Nat. Chem.* **10**, 740–745 (2018).
42. J. Cavanaugh, M. L. Whittaker, D. Joester, Crystallization kinetics of amorphous calcium carbonate in confinement. *Chem. Sci.* **10**, 5039–5043 (2019).
43. C. J. Stephens, S. F. Ladden, F. C. Meldrum, H. K. Christenson, Amorphous calcium carbonate is stabilized in confinement. *Adv. Funct. Mater.* **20**, 2108–2115 (2010).
44. S. M. Porter, Skeletal microstructure indicates chancelloriids and halkieriids are closely related. *Palaeontology* **51**, 865–879 (2008).
45. S. Bengtson, S. Conway Morris, B. J. Cooper, P. A. Jell, B. N. Runnegar, Early Cambrian fossils from South Australia. *Mem. Assoc. Australas. Palaeontol.* **9**, 1–364 (1990).
46. M. J. Vendrasco, S. M. Porter, A. Kouchinsky, G. Li, C. Z. Fernandez, New data on molluscs and their shell microstructures from the Middle Cambrian Gowers Formation, Australia. *Palaeontology* **53**, 97–135 (2010).
47. G. Giribet, New animal phylogeny: Future challenges for animal phylogeny in the age of phylogenomics. *Org. Divers. Evol.* **16**, 419–426 (2016).
48. M. dos Reis *et al*., Uncertainty in the timing of origin of animals and the limits of precision in molecular timescales. *Curr. Biol.* **25**, 2939–2950 (2015).
49. D. H. Erwin *et al*., The Cambrian conundrum: Early divergence and later ecological success in the early history of animals. *Science* **334**, 1091–1097 (2011).
50. A. Kouchinsky *et al*., Chronology of early Cambrian biomineralization. *Geol. Mag.* **149**, 221–251 (2012).